

Effect of grain size on gas bubble evolution in nuclear fuel: Phase-field investigations

Dan Sun(孙丹), Qingfeng Yang(杨青峰), Jiajun Zhao(赵家珺), Shixin Gao(高士鑫), Yong Xin(辛勇), Yi Zhou(周毅), Chunyu Yin(尹春雨), Ping Chen(陈平), Jijun Zhao(赵纪军), and Yuanyuan Wang(王园园)
Citation: Chin. Phys. B, 2024, 33 (**1**): 016105. DOI: 10.1088/1674-1056/ad08a6
Journal homepage: http://cpb.iphy.ac.cn; http://iopscience.iop.org/cpb

What follows is a list of articles you may be interested in

Structural, magnetic, and dielectric properties of Ni-Zn ferrite and Bi_2O_3 nanocomposites prepared by the sol-gel method

Jinmiao Han(韩晋苗), Li Sun(孙礼), Ensi Cao(曹恩思), Wentao Hao(郝文涛), Yongjia Zhang(张雍家), and Lin Ju(鞠林)
Chin. Phys. B, 2021, 30 (**9**): 096102. DOI: 10.1088/1674-1056/ac0904

Electrical properties of $Ca_{3-x}Sm_xCo_4O_{9+\delta}$ ceramics preparedunder magnetic field

Xiu-Rong Qu(曲秀荣), Yan-Yan Xu(徐岩岩), Shu-Chen Lü(吕树臣), Jian-Min Hu(胡建民)
Chin. Phys. B, 2020, 29 (**4**): 046103. DOI: 10.1088/1674-1056/ab75cb

Grain size and structure distortion characterization of α-MgAgSb thermoelectric material by powder diffraction

Xiyang Li(李西阳), Zhigang Zhang(张志刚), Lunhua He(何伦华), Maxim Avdeev, Yang Ren(任洋), Huaizhou Zhao(赵怀周), and Fangwei Wang(王芳卫)†
Chin. Phys. B, 2020, 29 (**10**): 106101. DOI: 10.1088/1674-1056/aba09c

Influence of nitrogen and magnesium doping on the properties of ZnO films

Dong-hua Li(李东华), Hui-Qiong Wang(王惠琼), Hua Zhou(周华), Ya-Ping Li(李亚平), Zheng Huang(黄政), Jin-Cheng Zheng(郑金成), Jia-Ou Wang(王嘉鸥), Hai-jie Qian(钱海杰), Kurash Ibrahim(奎热西), Xiaohang Chen(陈晓航), Huahan Zhan(詹华瀚), Yinghui Zhou(周颖慧), Junyong Kang(康俊勇)
Chin. Phys. B, 2016, 25 (**7**): 076105. DOI: 10.1088/1674-1056/25/7/076105

Tuning of magnetic properties of aluminium-doped strontium hexaferrite powders

Xiao-Mei Ma(马小梅), Jie Liu(刘杰), Sheng-Zhi Zhu(朱生志), Hui-Gang Shi(史慧刚)
Chin. Phys. B, 2016, 25 (**12**): 126102. DOI: 10.1088/1674-1056/25/12/126102

Effect of grain size on gas bubble evolution in nuclear fuel: Phase-field investigations

Dan Sun(孙丹)[1], Qingfeng Yang(杨青峰)[1], Jiajun Zhao(赵家珺)[2], Shixin Gao(高士鑫)[1], Yong Xin(辛勇)[1], Yi Zhou(周毅)[1], Chunyu Yin(尹春雨)[1], Ping Chen(陈平)[1,†], Jijun Zhao(赵纪军)[2], and Yuanyuan Wang(王园园)[2,‡]

[1] *Science and Technology on Reactor System Design Technology Laboratory, Nuclear Power Institute of China, Chengdu* 610213, *China*
[2] *Key Laboratory of Materials Modification by Laser, Ion, and Electron Beams, Dalian University of Technology, Dalian* 116024, *China*

(Received 3 August 2023; revised manuscript received 28 September 2023; accepted manuscript online 2 November 2023)

Numerous irradiation-induced gas bubbles are created in the nuclear fuel during irradiation, leading to the change of microstructure and the degradation of mechanical and thermal properties. The grain size of fuel is one of the important factors affecting bubble evolution. In current study, we first predict the thermodynamic behaviors of point defects as well as the interplay between vacancy and gas atom in both UO_2 and U_3Si_2 according to *ab initio* approach. Then, we establish the irradiation-induced bubble phase-field model to investigate the formation and evolution of intra- and inter-granular gas bubbles. The effects of fission rate and temperature on the evolutions of bubble morphologies in UO_2 and U_3Si_2 have been revealed. Especially, a comparison of porosities under different grain sizes is examined and analyzed. To understand the thermal conductivity as functions of grain size and porosity, the heat transfer capability of U_3Si_2 is evaluated.

Keywords: grain size, point defects, fission gas bubble

PACS: 61.72.Mm, 61.72.J–, 61.72.–y **DOI:** 10.1088/1674-1056/ad08a6

1. Introduction

Since the Fukushima accident occurs, the development of accident-tolerant fuels (ATFs) has been a more prominent topic of interest for improving the safety, competitiveness and economics of commercial nuclear power.[1] Large-grained UO_2 is a promising candidate to replace the traditional UO_2 fuel, as its larger grain size may reduce irradiation-induced swelling and fission gas release.[2] In addition, U_3Si_2 fuel is also a potentially attractive substitute for commercial UO_2 fuel due to its higher thermal conductivity and uranium density.[2] These excellent properties can not only extend the refuelling cycle but also have a promising potential in reducing fuel enrichment.[3,4] Recently, more attention has been paid on the irradiation swelling behavior of large-grained UO_2 and U_3Si_2.

Noirot *et al.*[5] compared the microstructures of coarse-grained UO_2 and conventional-grained UO_2 at the burnups of 72 GWd/tHM and 76 GWd/tHM, respectively. The bubbles and grain refinement were observed in the standard-grained UO_2, while in the large-grained UO_2, bubbles only formed at the center of grains and on the grain boundaries (GBs), indicating that coarse grains can effectively improve the irradiation resistance of UO_2. The irradiation experiments performed by AREVA[6,7] indicate that fission gas release and fuel swelling are reduced by doping Cr_2O_3 in the large-grained UO_2. In the Cr_2O_3-doped UO_2 with large grain size, fission gas is mainly dissolved in the grains rather than on the GBs, which is different from that in the conventional-grained UO_2. It can be attributed to the fact that the larger grain size increases the diffusion distance of fission gas from grain interior to GB, improving irradiation swelling resistance. Cooper *et al.*[8] investigated the influence of Cr on the diffusion rate of Xe atom in UO_2 using the cluster dynamics method, which is called by the BISON program to study the behavior of fission gas release in the doped UO_2.

Moreover, the irradiation properties of U_3Si_2 are examined and analyzed. According to the microstructure of irradiated U_3Si_2/Al dispersion fuel, the fission bubbles are uniformly distributed within the U_3Si_2 fuel particles. The mean diameter of bubbles is approximately 94 nm, leading to $\sim 11\%$ increase of the volume fraction.[9] Taking account of the experimental results of irradiated U_3Si_2 fuel in the light water reactor,[10,11] the bubble density and size are assessed by a fission gas model. It is assumed that fission gas release is controlled by the bubbles on the GB, and the sensitivity of the model parameters is additionally analyzed. On the other hand, a rate theory model of fission gas behavior is developed and applied to explore the swelling of U_3Si_2 fuel.[12] The amorphous U_3Si_2 fuel has also been observed under irradiation, and hence, Rest[13] established a model to study the behavior of fission gas bubble in the amorphous U_3Si_2.

†Corresponding author. E-mail: Chenping_npic@163.com
‡Corresponding author. E-mail: yuanyuanwang@dlut.edu.cn

© 2024 Chinese Physical Society and IOP Publishing Ltd

Despite the extensive research has been carried out on the irradiation performance of large-grained UO_2 and U_3Si_2, to authors' knowledge, the evolution of fission gas bubble in UO_2 and U_3Si_2 fuels associated with different grain sizes under different fission rates and temperatures is still waiting to be identified. Nowadays, at the atomic scale, *ab initio* is widely used to simulate the thermal dynamics behaviors of irradiation-induced point defects (*i.e.*, vacancy and self-interstitial atom) and fission gas atom in both UO_2 and U_3Si_2.[14–16] The phase-field approach considered as a typical mesoscopic method is employed to understand the formation and growth of bubbles and the gas swelling in the nuclear fuel.[17–20] For examples, Aagesen *et al.*[18] established a phase-field model by tracking the concentrations of vacancy and gas atom to simulate the fission bubbles in UO_2 fuel. Wang *et al.*[19] investigated the effects of vacancy concentration, the generation rate of Xe atom and the temperature gradient on the evolution of bubbles in UO_2 by means of the phase-field model. In addition, the morphology structure of intergranular fission gas bubbles in U_3Si_2 is also investigated using the phase-field method.[20]

Hence, in current work, *ab initio* calculation is first performed to obtain the energetic values (e.g., formation energy) of vacancy, self-interstitial and fission gas atom in U_3Si_2 and UO_2, respectively. A comparison of bubble density, size and porosity of U_3Si_2 and UO_2 is presented under different temperatures and fission rates. The difference of bubble evolution characteristics under different grain sizes is shown. Moreover, the corresponding thermal conductivities of bubble-containing U_3Si_2 are evaluated by the established steady heat transfer model. The predicted results can provide fundamental understanding on the mechanics of bubble formation and evolution, which is helpful for the future research on the irradiation swelling of U_3Si_2 and UO_2 fuels.

2. Computational framework

2.1. Point defect energies from atomic simulation

All the calculations are performed within the framework of density functional theory (DFT) using the projector augmented wave method implemented in Vienna *ab initio* simulation package (VASP).[21] We adopt the projector-augmented wave (PAW) potentials for the ion–electron interaction.[22] The generalized gradient approximation (GGA) in the parameterization by Perdew, Burke, and Ernzerh (PBE) of functional is used to describe the electron exchange–correlation interactions.[23] Moreover, the effects due to the localization of 5f electrons of uranium in UO_2 and U_3Si_2 were treated with the GGA$+U$ approximation, the value of U_{eff} is set as 4 eV for both UO_2 and U_3Si_2.[24–26] The calculated equilibrium lattice constants of UO_2 ($a = c = 5.57$ Å, $b = 5.50$ Å) are in reasonable agreement with the experiment data[27] and previous theoretical values.[28] The lattice constants of U_3Si_2 ($a = b = 7.33$ Å, $c = 3.90$ Å) are using the experiment data.[29] The structures of UO_2 and U_3Si_2 have been presented in Fig. 1, respectively. We use a 96-atom UO_2 supercell formed by $2\times2\times2$ unit cells and a 160-atom U_3Si_2 supercell formed by $2\times2\times4$ unit cells. The cutoff energy of plane wave is set as 500 eV. The Brillion zone integrations for UO_2 and U_3Si_2 are performed using $4\times4\times5$ and $3\times3\times3$ Monkhorst–Pack grid, respectively. All atomic positions are fully relaxed at the constant volume until the energy variation on each atom is less than 1×10^{-4} eV and the total force on each atom is less than 0.01 eV/Å.

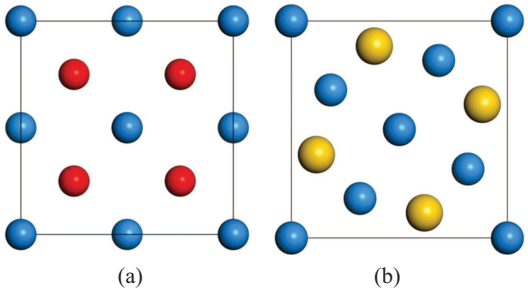


Fig. 1. Structures of UO_2 and U_3Si_2 crystals. Red ball represents O atom, blue ball represents U atom, and yellow ball represents Si atom.

The formation energies (E^{f}) of vacancy and Xe atom in UO_2 and U_3Si_2 are defined as

$$E^{\text{f}}_{\text{vacancy}} = E_{\text{total}} - E_0 + \mu_X, \tag{1}$$

$$E^{\text{f}}_{\text{Xe(interstitialy)}} = E_{\text{total}} - E_0 + \mu_{\text{Xe}}, \tag{2}$$

$$E^{\text{f}}_{\text{Xe(interstitialy)}} = E_{\text{total}} - \mu_{\text{Xe}} + \mu_X. \tag{3}$$

Here, E_{total} is the energy of the supercell containing a defect, μ denotes the chemical potential of atom in the most stable site, and therefore μ_{Xe} is the energy of an isolated Xe atom in a large empty supercell, μ_{O} is one half of the energy of a gas-phase O_2 molecule in a large empty supercell, μ_{U} and μ_{Si} are the energy per U/Si atom in the corresponding bulk phase, E_0 is the total energy of UO_2/U_3Si_2 supercell. By definition, a system with the positive formation energy means its formation process is endothermic, while the negative value to formation energy means exothermic.

2.2. Phase-field model

To explore the evolution features of intra- and intergranular bubbles in both UO_2 and U_3Si_2, the phase-field model is developed.[30–32] The total free energy of the polycrystalline system is written as

$$F(c,\eta) = N\int \Big((1-h(\eta)) f^{\mathrm{m}}(c) + h(\eta) f^{\mathrm{b}}(c) + f^{\mathrm{pc}}(\eta, \phi_{1\to p}) + \omega_0 g(c,\eta) + \kappa_{\mathrm{v}} |\nabla c_{\mathrm{v}}|^2 + \kappa_{\mathrm{i}} |\nabla c_{\mathrm{i}}|^2 + \kappa_{\mathrm{g}} |\nabla c_{\mathrm{g}}|^2 + \kappa_{\eta} |\nabla \eta|^2 \Big) \mathrm{d}V. \tag{4}$$

Here, η and ϕ are the order parameters to distinguish the bubble phase and matrix phase and to identify different grains, respectively. Especially, η equaled to 1 represents the bubble phase, and η equaled to 0 represents the matrix phase. P is the number of possible orientations in space, and ϕ_i $(i = 1, \ldots, p)$ are the orientation field variables. Across the GBs between the grain ϕ_i and its neighborhood grain, the absolute value of ϕ_i varies continuously from 1 to 0.

The free energy of the matrix (f^{m}) is expressed as

$$\begin{aligned} f^{\mathrm{m}} = {} & (c_{\mathrm{v}} - c_{\mathrm{v}}^{\mathrm{eq}}) \left(E_{\mathrm{v}}^{\mathrm{f}} - T S_{\mathrm{v}}^{\mathrm{f}} \right) + (c_{\mathrm{i}} - c_{\mathrm{i}}^{\mathrm{eq}}) \left(E_{\mathrm{i}}^{\mathrm{f}} - T S_{\mathrm{i}}^{\mathrm{f}} \right) + (c_{\mathrm{g}} - c_{\mathrm{g}}^{\mathrm{eq}}) \left(E_{\mathrm{g}}^{\mathrm{f}} - T S_{\mathrm{g}}^{\mathrm{f}} \right) \\ & + k_{\mathrm{B}} T \left((1 - c_{\mathrm{v}} - c_{\mathrm{i}} - c_{\mathrm{g}}) \ln (1 - c_{\mathrm{v}} - c_{\mathrm{i}} - c_{\mathrm{g}}) - (1 - c_{\mathrm{v}}^{\mathrm{eq}} - c_{\mathrm{i}}^{\mathrm{eq}} - c_{\mathrm{g}}^{\mathrm{eq}}) \ln (1 - c_{\mathrm{v}}^{\mathrm{eq}} - c_{\mathrm{i}}^{\mathrm{eq}} - c_{\mathrm{g}}^{\mathrm{eq}}) \right. \\ & \left. + c_{\mathrm{v}} \ln c_{\mathrm{v}} - c_{\mathrm{v}}^{\mathrm{eq}} \ln c_{\mathrm{v}}^{\mathrm{eq}} + c_{\mathrm{i}} \ln c_{\mathrm{i}} - c_{\mathrm{i}}^{\mathrm{eq}} \ln c_{\mathrm{i}}^{\mathrm{eq}} + c_{\mathrm{g}} \ln c_{\mathrm{g}} - c_{\mathrm{g}}^{\mathrm{eq}} \ln c_{\mathrm{g}}^{\mathrm{eq}} \right), \end{aligned} \tag{5}$$

where f^{b} is the free energy of the gas bubble and is expressed by the simplified van der Waals equation of state in the following equation:

$$\begin{aligned} f^{\mathrm{b}} = {} & \left[(c_{\mathrm{v}} - 1)^2 + c_{\mathrm{i}}^2 \right] + \left[\mu_{\mathrm{g}}^0 c_{\mathrm{g}}^{\mathrm{b}} + c_{\mathrm{g}}^{\mathrm{b}} k_{\mathrm{B}} T \ln c_{\mathrm{g}}^{\mathrm{b}} + c_{\mathrm{g}}^{\mathrm{b}} k_{\mathrm{B}} T \ln \left(\frac{k_{\mathrm{B}} T}{p_0} \right) \right. \\ & \left. - c_{\mathrm{g}}^{\mathrm{b}} k_{\mathrm{B}} T \ln (1 - A' c_{\mathrm{g}}^{\mathrm{b}} k_{\mathrm{B}} T) + A' c_{\mathrm{g}}^{\mathrm{b}} k_{\mathrm{B}} T \left(\frac{c_{\mathrm{g}}^{\mathrm{b}} k_{\mathrm{B}} T}{1 - A' c_{\mathrm{g}}^{\mathrm{b}} k_{\mathrm{B}} T} - p_0 \right) \right], \end{aligned} \tag{6}$$

where A' is a constant fitted based on the experimental data, p_0 is the reference pressure, $c_{\mathrm{g}}^{\mathrm{b}}$ is the atomic concentration of gas atom in the bubble. The definition of $c_{\mathrm{g}}^{\mathrm{b}}$ is given as

$$c_{\mathrm{g}}^{\mathrm{b}} = \frac{n}{V_{\mathrm{b}}} = \frac{n}{N_{\mathrm{V}} V_{\mathrm{site}}} = \frac{n}{N_{\mathrm{site}}} \frac{1}{V_{\mathrm{site}}} = c_{\mathrm{g}} \frac{1}{V_{\mathrm{site}}}, \tag{7}$$

where n is the number of Xe atom in a bubble, V_{b} is the volume of bubble, N_{V} is the number of vacancies, and V_{site} is the volume of crystal lattice.

The reference pressure is expressed as

$$p_0 = \frac{c_{\mathrm{g}} (1/V_{\mathrm{site}}) k_{\mathrm{B}} T}{1 - A' c_{\mathrm{g}} (1/V_{\mathrm{site}}) k_{\mathrm{B}} T}. \tag{8}$$

In current work, the simplified van der Waals equation of state is used and its expression is

$$p = \frac{RT}{V_{\mathrm{g}}} \left(1 + \frac{c}{V_{\mathrm{g}} - b} \right) - \frac{a}{V_{\mathrm{g}}^2}. \tag{9}$$

According to Ref. [33], parameters a, b, and c are determined as 259780 J·cm^3/mol^2, 23.9276 J·cm^3/mol^2, and 55.6583 J·cm^3/mol^2, respectively.

To predict the intergranular bubble evolution, the effect of polycrystalline free energy is considered, and f^{pc} is expressed as follows:

$$f^{\mathrm{pc}}(\eta, \phi_{1\to p}) = 3A \left(\sum_{k=1}^{p} \phi_k^2 + \eta^2 \right)^2 - 4A \left(\sum_{k=1}^{p} \phi_k^3 + \eta^3 \right). \tag{10}$$

The concentrations of vacancy (c_{v}), self-interstitial (c_{i}), and gas atom (c_{g}) as a function of time are given as

$$\frac{\partial c_{\mathrm{v}}}{\partial t} = \nabla \left(M_{\mathrm{v}} \nabla \frac{\partial F}{\partial c_{\mathrm{v}}} \right) + P_{\mathrm{v}} - R_{\mathrm{v,i}}, \tag{11}$$

$$\frac{\partial c_{\mathrm{i}}}{\partial t} = \nabla \left(M_{\mathrm{i}} \nabla \frac{\partial F}{\partial c_{\mathrm{i}}} \right) + P_{\mathrm{i}} - R_{\mathrm{v,i}}, \tag{12}$$

$$\frac{\partial c_{\mathrm{g}}}{\partial t} = \nabla \left(M_{\mathrm{g}} \nabla \frac{\partial F}{\partial c_{\mathrm{g}}} \right) + P_{\mathrm{g}}, \tag{13}$$

$$\frac{\partial \eta}{\partial t} = -L \frac{\partial F}{\partial \eta}. \tag{14}$$

Here, M is the migration rate of defect ($M_m = D_m c_m / k_{\mathrm{B}} T$ with $m =$ v i, and g), where D is the diffusion coefficient, P is the generation rate of defect, and $R_{\mathrm{v,i}}$ is the recombination rate between the vacancy and the self-interstitial atom. All the performances are carried out in a $256\Delta x \times 256\Delta y$ simulation domain. The formation energies of defects are obtained by using *ab initio* calculations in the present work and the other parameters are summarized in the following Table 1. The periodic boundary condition is applied to the simulation domain and we use the normalization parameters for the numerical calculation: $l^* = 1$ nm, $t^* = 0.1$ s.

Table 1. Parameters used for phase-field simulations.

Parameters	UO_2	U_3Si_2
T	1200 K/1773 K/2073 K	473 K/673 K/873 K
γ	1.72 eV[34]	1.72 eV[34]
a_0	5.57 Å	7.33 Å
D_V	1.9×10^{-17} m^2/s (1200 K)	1.48×10^{-24} m^2/s (473 K)
	2.25×10^{-14} m^2/s (1773 K)	2.56×10^{-19} m^2/s (673 K)
	3.01×10^{-13} m^2/s (2073 K)[14]	1.76×10^{-16} m^2/s (873 K)[14]
D_i	4.4×10^{-16} m^2/s (1200 K)	3.71×10^{-21} m^2/s (473 K)
	1.62×10^{-13} m^2/s (1773 K)	1.29×10^{-16} m^2/s (673 K)
	1.4×10^{-12} m^2/s (2073 K)[14]	3.71×10^{-14} m^2/s (873 K)[14]
D_{Xe}	D_V	D_V
$\dot{F}$	1.09×10^{18} m^{-3}·s^{-1}	3×10^{20} m^{-3}·s^{-1}
	2.09×10^{18} m^{-3}·s^{-1}	5×10^{20} m^{-3}·s^{-1}
	3.09×10^{18} m^{-3}·s^{-1}	7×10^{20} m^{-3}·s^{-1}

3. Results and discussion

3.1. Formation energies of point defects and Xe atom

First, we compare the possible configurations and stabilities of intrinsic point defects in UO_2 and U_3Si_2 host crystal. Four types of point defects in UO_2 (that is U vacancy (V_U), O vacancy (V_O), U interstitial (I_U), O interstitial (I_O)), and five types of point defects in U_3Si_2 (that is two different U vacancies marked as V_{U1} and V_{U2}, where U1 and U2 represent the occupied positions in the minimum symmetric cell with U 4*h* (0.181, 0.681, 0.5) and U 2*a* (0, 0, 0), respectively, Si vacancy (V_{Si1}), U interstitial (I_U), and Si interstitial (I_{Si})) are considered. The formation energies of these point defects are summarized in Fig. 2.

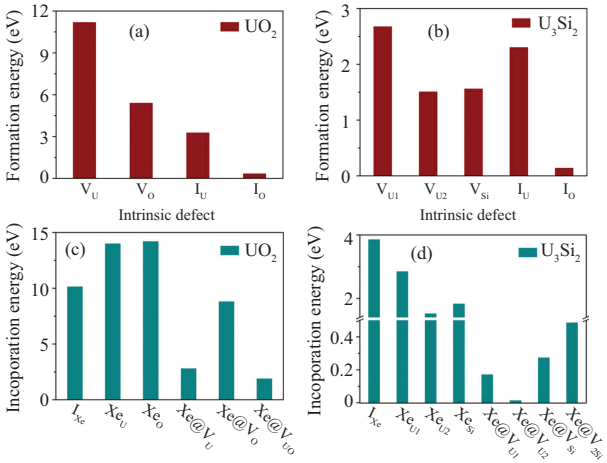


Fig. 2. Formation energies of irradiation-induced point defects in (a) UO_2 and (b) U_3Si_2 crystals, respectively, and the incorporation energy of Xe atom in (c) UO_2 and (d) U_3Si_2 crystals, respectively.

As shown in Fig. 2(a), the stabilities of intrinsic defects in UO_2 increase in an order of I_O, I_U, V_O, and V_U, and the corresponding formation energies are 0.34 eV, 3.27 eV, 5.40 eV, and 11.19 eV, respectively. While the stabilities of intrinsic defects in U_3Si_2 increase in an order of I_{Si}, V_{U2}, V_{Si}, I_U, and V_{U1}. Among the values of formation energies, E^f of U vacancy in UO_2 is the highest one, and the value of V_{U2} in U_3Si_2 is the lowest one. From the energetic point, O interstitial first forms in UO_2 than other intrinsic defects, while in U_3Si_2, the formations of U vacancy and Si interstitial are more energetically favorable than those of other intrinsic defects.

To further reveal different thermodynamic behaviors of fission gas bubbles between UO_2 and U_3Si_2, we analyze the incorporation energy of Xe and the interaction between vacancy and Xe. The Xe atom occupied the interstitial site (I_{Xe}) and the substitutional site (Xe_X, X represents U, O or Si atoms) is considered here. As shown in Fig. 2(c), the incorporation energy of I_{Xe} in UO_2 is lower than those of Xe_U and Xe_O. Nevertheless, in U_3Si_2, the opposite result is obtained that Xe on the U2 site shows the most stable status. Then, we compare the stabilities of Xe–vacancy complexes in UO_2 and U_3Si_2. It should be noted that there are many types of divacancy in UO_2 and U_3Si_2, and we only consider the most stable divacancy. The most stable double vacancy in UO_2 is composed of one O vacancy and one U vacancy (V_{UO}) and that in U_3Si_2 is composed of two Si vacancies (V_{2Si}). In UO_2, the incorporation energies of Xe occupied the sites of single vacancy (V_O and V_U) and divacancy (V_{UO}) are much lower than that of Xe at the interstitial site, especially the V_{UO} site. On the contrary, in U_3Si_2, the energy of Xe atom incorporated with divacancy is higher than that with monovacancy. A comparison of the incorporation energies in UO_2 and U_3Si_2 indicates that Xe atom is more stable in U_3Si_2 than that in UO_2.

3.2. Fission gas bubble and its effect on thermal conductivity

3.2.1. Intragranular bubble

Different temperatures and fission densities influence the formation characteristics of gas bubble (i.e., the density and size of gas bubbles) in the nuclear fuel. This is due to the temperature-dependent materials' parameters and the external

irradiation environment. For UO_2, we choose 1200 K, 1773 K, and 2073 K as the representative temperatures to understand the effect of temperature on the bubble evolution, and three different temperatures at 473 K, 673 K, and 873 K are assumed to reveal the temperature impact on bubble formation in U_3Si_2. Figures 3 and 4 show the bubble morphologies in UO_2 and U_3Si_2 as functions of time and temperature, respectively. The morphologies of UO_2 and U_3Si_2 after irradiation show that the intragranular bubbles are generally formed.[35–37] Our simulation results are in good agreement with the experimental results.

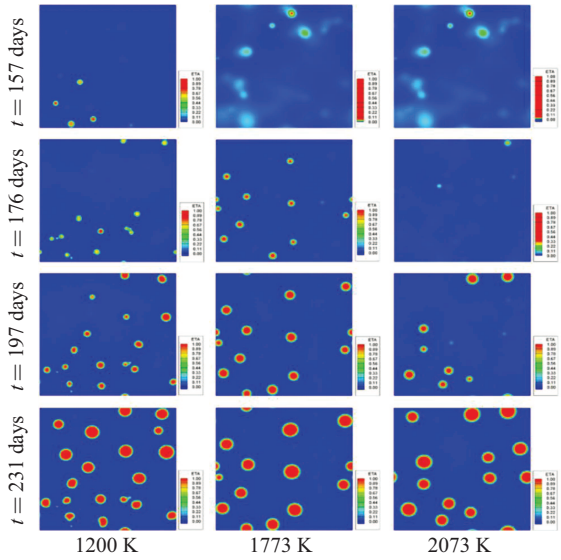


Fig. 3. Morphologies of intragranular bubbles as a function of temperature in UO_2 under different time points.

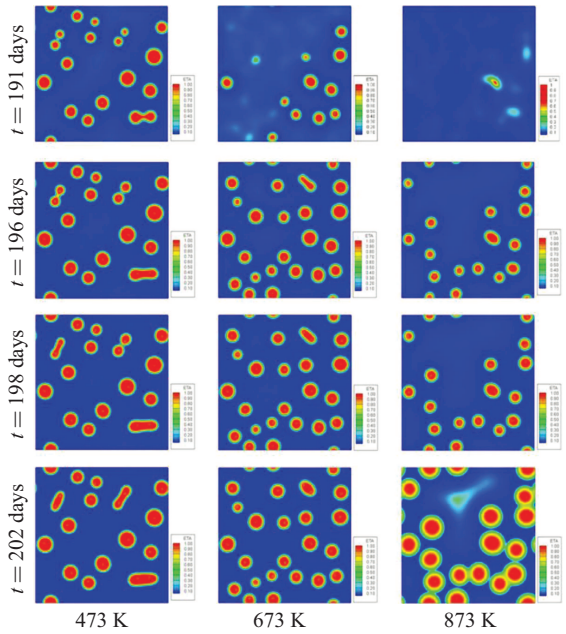


Fig. 4. Morphologies of intragranular bubble as a function of temperature in U_3Si_2 at different time points.

With time increasing, both number and size of bubble increase. At the same time, their differences determined by temperature are obviously captured. In Fig. 5, the density, size and porosity of intragranular bubbles in UO_2 and U_3Si_2 varied with time are plotted respectively. Generally speaking, three stages of bubble density can be divided, that is incubation stage, formation and growth stage and coarsening stage. In each stage, obvious features are shown. At the incubation stage, there is no bubble in the matrix. A dramatic increase of bubble number occurs at the formation and growth stage, and then the number of bubbles keep almost unchanged at a longer time. Compared with the incubation stage at a lower temperature, higher temperature leads to longer incubation time. As is known, the gas atoms, vacancies and self-interstitial atoms experience the generation, diffusion, aggregation, recombination and annihilation to form individual gas bubbles, and the bubble connection would occur with increasing time. The temperature-dependent material parameters influence the formation time of bubble. The formation of bubble becomes more difficult at higher temperature since the energetic value and the defect diffusion coefficient are higher.

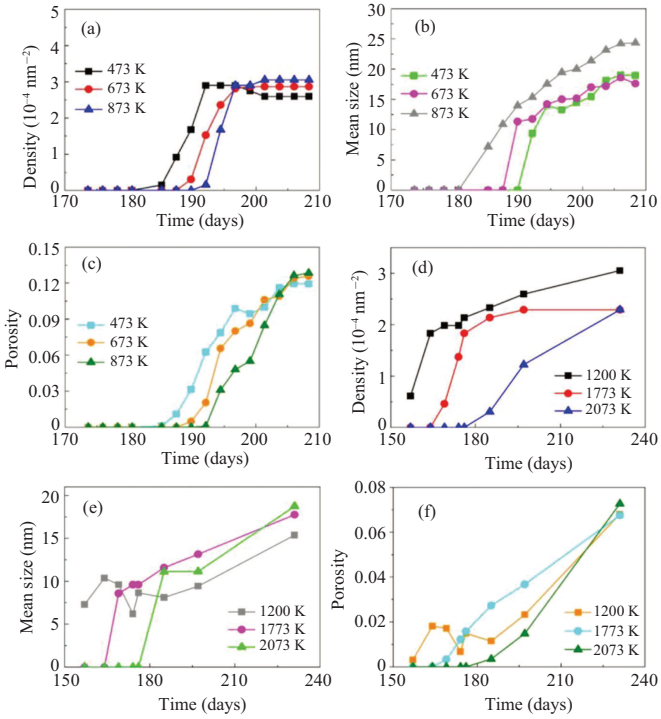


Fig. 5. Comparison of intragranular bubble density, size, and porosity at different temperatures in (a)–(c) UO_2 and (d)–(f) U_3Si_2.

For UO_2, the bubble density at 1200 K is higher than those at both 1773 K and 2073 K (Fig. 5(a)), and the mean size of gas bubble at 1773 K shows the highest value than those at other temperatures (Fig. 5(b)). To assess the porosity, the bubble size and density are simultaneously considered. The maximal porosity occurs at 1773 K and the minimal one presents at 2073 K if the time is in a range of 180 days to 220 days (Fig. 5(c)). For U_3Si_2, lower temperature reaches to the coarsening stage earlier than that at higher temperature in

Fig. 5(d), and the maximal and minimal bubble densities appear at 873 K and 473 K, respectively. Overall speaking, in Fig. 5(e), the mean size of bubble at 873 K shows the largest one, and the smallest size presents at 473 K. As for a comparison of porosity in Fig. 5(f), the highest one and the lowest one appear at 473 K and 873 K, respectively.

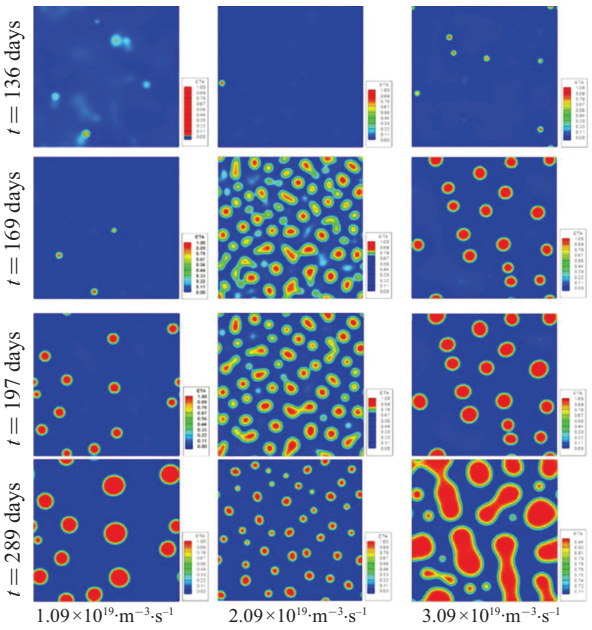


Fig. 6. Morphologies of intragranular bubble as a function of fission rate in UO_2 at different time points.

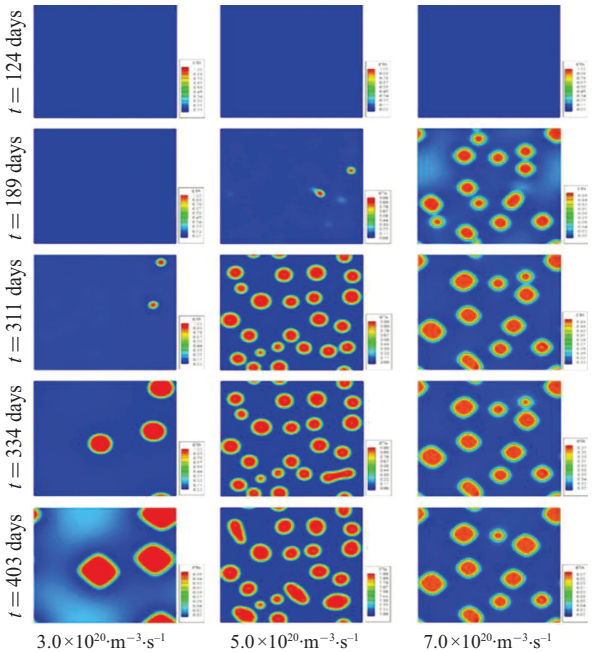


Fig. 7. Morphologies of intragranular bubble as a function of fission rate in U_3Si_2 at different time points.

In addition to temperature effect, higher fission rate indicates there will be more point defects generated in the fuel, facilitating the formation of more bubbles. In the following investigation, the fission rates of 1.09×10^{19} $m^{-3}{\cdot}s^{-1}$, 2.09×10^{19} $m^{-3}{\cdot}s^{-1}$, and 3.09×10^{19} $m^{-3}{\cdot}s^{-1}$ for UO_2 and 3.0×10^{20} $m^{-3}{\cdot}s^{-1}$, 5.0×10^{20} $m^{-3}{\cdot}s^{-1}$, and 7.0×10^{20} $m^{-3}{\cdot}s^{-1}$ for U_3Si_2 are assumed and performed on the phase-field simulation. As the microstructures shown in Figs. 6 and 7, lower fission rate results in longer bubble incubation time in UO_2 and U_3Si_2. It can be attributed to the face that the number of point defects produced by lower fission rate is smaller than that by higher fission per unit time and per unit space. Yao *et al.*[38] investigated the irradiation behavior of U_3Si_2 under 300-keV Xe^+ ion beam bombardment, and the results shown that the formation and coalescence of Xe bubble increase with an increment of irradiation dose.

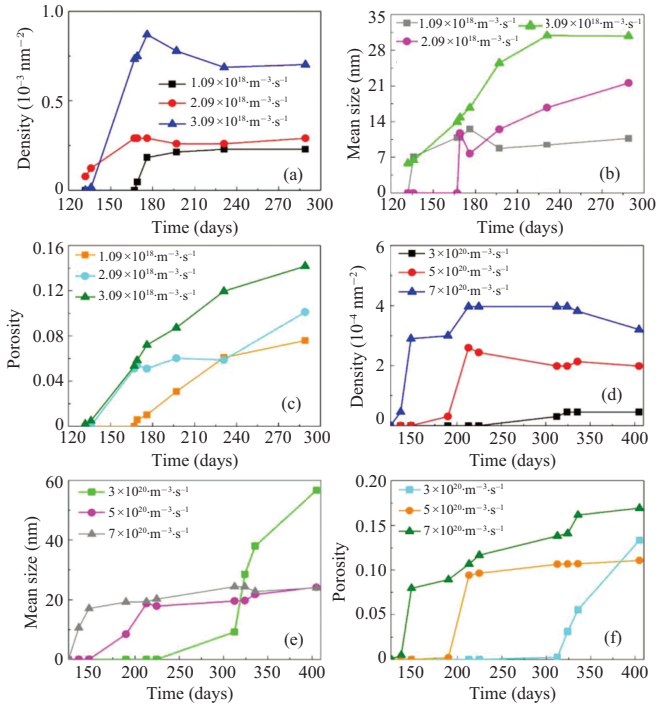


Fig. 8. Comparison of intragranular bubble density, size, and porosity at different fission rates in (a)–(c) UO_2 and (d)–(f) U_3Si_2.

To quantitatively investigate the influence of fission rate, the bubble density, size and porosity as a function of time are evaluated. The corresponding results of UO_2 and U_3Si_2 are plotted in Fig. 8, respectively. There is no doubt that bubble density, size and porosity in UO_2 increase with the fission rate increase. The value of bubble size at 3.09×10^{18} $m^{-3}{\cdot}s^{-1}$ is much higher than those at other fission rates. However, for U_3Si_2, the bubble size increases with increasing fission rate if the evolution time is less than 316 days as shown in Fig. 8(e). Once the time is greater than 316 days, the bubble size at 3.0×10^{20} $m^{-3}{\cdot}s^{-1}$ increases dramatically as high as 58 nm. The bubble density increases with the increment of fission rate as shown in Fig. 8(d). The porosity of U_3Si_2 in Fig. 8(f) illustrates that the increment of fission rate can lead to higher porosity. Compared with the experimentally measured data,[37] the predicted porosity of U_3Si_2 is consistent with the evolution trend, which is shown in Fig. 9.

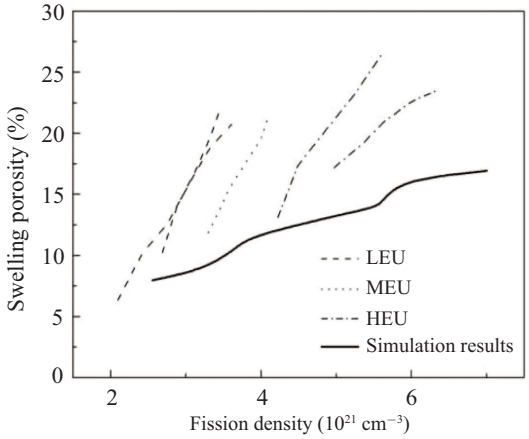


Fig. 9. Predicted porosity in U_3Si_2 versus previous experimentally measured data.[29] LEU represents low enriched uranium, MEU represents medium enriched uranium, HEU represents highly enriched uranium.

The bubble-containing microstructure can highly degrade the thermal property since the heat transfer capability of gas is much lower than that of solid matrix. To evaluate the effect of Xe gas-filled bubble on the thermal conductivity, the steady heat transfer according to the Fourier's law is utilized. The effective thermal conductivity is expressed as

$$\kappa^{\text{eff}} = \frac{\bar{J}}{(\mathrm{d}T/\mathrm{d}r)}. \tag{15}$$

Here, $\bar{J}$ is the average heat flux per unit area, $\mathrm{d}T/\mathrm{d}r$ is the mean temperature gradient along the r direction. To numerically solve Eq. (15), the finite difference method is used. To authors' knowledge, the temperature-dependent thermal conductivity of U_3Si_2 is[39]

$$K_{U_3Si_2} = 3.605 + 1.568\times10^{-2}T - 2.230\times10^{-6}T^2 + 1.655\times10^{-10}T^3. \tag{16}$$

The temperature-dependent thermal conductivity of Xe is[40]

$$K_{\text{Xe}} = 6.49\times10^{-4} + 1.794\times10^{-5}T - 2.343\times10^{-9}T^2. \tag{17}$$

Therefore, the thermal conductivities of U_3Si_2 at 473 K, 673 K, and 873 K are 10.540 W/m·K, 13.198 W/m·K, and 15.704 W/m·K, respectively, and those of Xe at 473 K, 673 K, and 873 K are 0.00861 W/m·K, 0.01166 W/m·K, and 0.01452 W/m·K, respectively. From the comparison of thermal conductivities, it is found that the thermal conductivity of U_3Si_2 is 3–4 orders of magnitude higher than that of Xe. According to the existing thermal conductivity model,[41] the variation rule of thermal conductivity can be described by the empirical formula $K = K_0(1+P)^{\varepsilon}$, where K_0 is the thermal conductivity of the matrix, P is the porosity, ε is the fitting parameter. Accordingly, the expression of thermal conductivity can be extended to

$$K = \left(3.605 + 1.568\times10^{-2}T - 2.230\times10^{-6}T^2 + 1.655\times10^{-10}T^3\right)(1+P)^{-1.89}. \tag{18}$$

Figure 10(a) shows the comparison between the simulated results and the fitting data. It confirms that the empirical model can well describe the thermal conductivity evolution with changing porosity. From the predicted results, the thermal conductivity decreases linearly with the increase of porosity, and the overall thermal conductivity increases with increasing temperature as expected.

The thermal conductivity of U_3Si_2 under different fission rates (e.g., 3.0×10^{20} m^{-3}·s^{-1}, 5.0×10^{20} m^{-3}·s^{-1}, and 7.0×10^{20} m^{-3}·s^{-1}) can also be fitted by the empirical formula $K = K_0(1+P)^{\varepsilon}$, and the corresponding expression is shown in the following format:

$$K = \left(3.605 + 1.568\times10^{-2}T - 2.230\times10^{-6}T^2 + 1.655\times10^{-10}T^3\right) \times\left[1 + 0.165\left(1-\exp(-0.0181(t-269)^{1.0})\right)\right]^{-1.89}, \tag{19}$$

$$K = \left(3.605 + 1.568\times10^{-2}T - 2.230\times10^{-6}T^2 + 1.655\times10^{-10}T^3\right) \times\left[1 + 0.107\left(1-\exp(-0.101(t-190)^{0.93})\right)\right]^{-1.89}, \tag{20}$$

$$K = \left(3.605 + 1.568\times10^{-2}T - 2.230\times10^{-6}T^2 + 1.655\times10^{-10}T^3\right) \times\left[1 + 0.194\left(1-\exp(-0.102(t-136)^{0.5})\right)\right]^{-1.89}. \tag{21}$$

To further consider the effect of fission rate on thermal conductivity, the formula can be derived into $K = K_0(1+P)(A\dot{f}+B)$, where A and B are fitting parameters and $\dot{f}$ is the fission rate. On a basis of the simulated thermal conductivity, the thermal conductivity can be fitted as follows:

$$K = \left(3.605 + 1.568\times10^{-2}T - 2.230\times10^{-6}T^2 + 1.655\times10^{-10}T^3\right)\times(1+P)\left(-7.12\times10^{-22}\dot{f} + 1.1\right). \tag{22}$$

Figure 10(b) presents our predicted effective thermal conductivity of U_3Si_2 using the classical Fourier's law, compared with the data calculated from Eq. (22). It shows that the results match well with each other from these two simulation and modeling approaches, and the effective thermal conductivity as a function of fission rate decreases linearly since a higher fission rate leads to more generation of gas bubble.

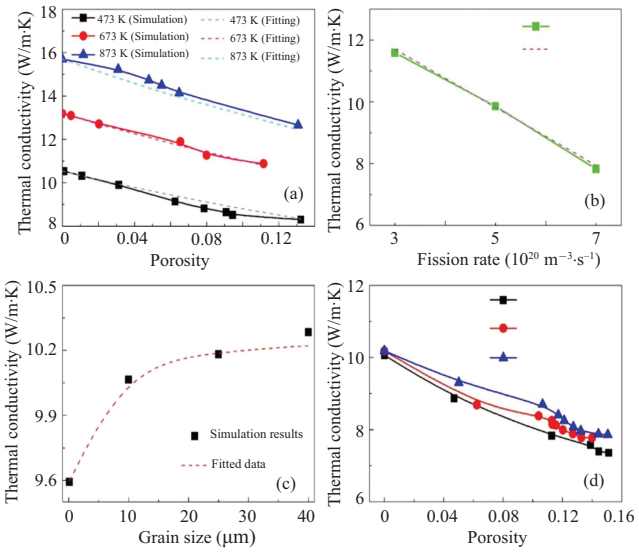


Fig. 10. Thermal conductivity predictions of bubble-containing U_3Si_2 vary with (a) porosity and (b) fission rate, and predicted thermal conductivity as functions of (c) grain size and (d) porosity in polycrystalline U_3Si_2.

3.2.2. Intergranular bubble

GB is usually considered as the trapping position to vacancies, self-interstitial and gas atoms. Hence, the grain size plays an important role in the evolution of bubble. In this section, we investigated the interaction between GB and gas bubble in UO_2 and U_3Si_2 with three different grain sizes (i.e., 10 μm, 25 μm, and 40 μm). The evolutions of intergranular bubbles in UO_2 and U_3Si_2 are shown in Figs. 11 and 12, respectively.

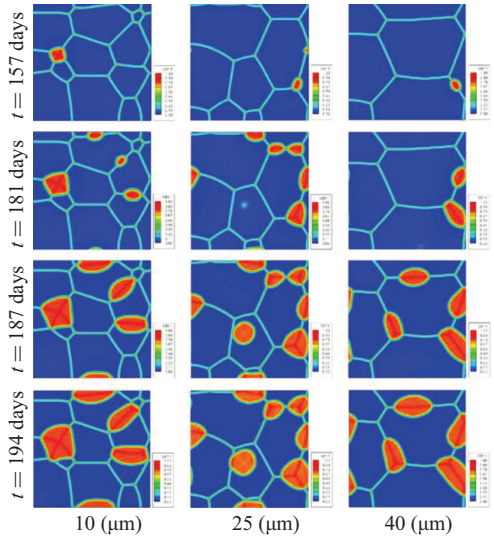


Fig. 11. Morphologies of intergranular bubble as a function of grain size in UO_2 under different time points.

A remarkable characteristic is captured that gas bubbles preferentially form at the trigonal GBs regardless of fuel type. This is because the incorporation energies of defects at the trigonal GBs are much lower, where point defects tend to cluster. On the other hand, bubbles formed on the straight GBs tend to be elliptical shape, which is closely related to minimize the interface energy between bubble surface and matrix.

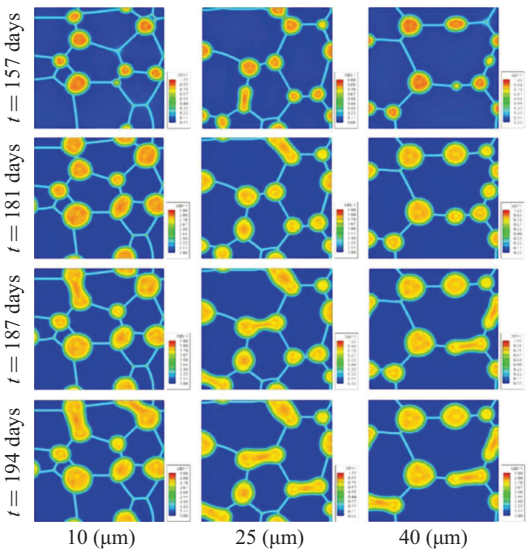


Fig. 12. Morphologies of intergranular bubble as a function of grain size in U_3Si_2 under different time points.

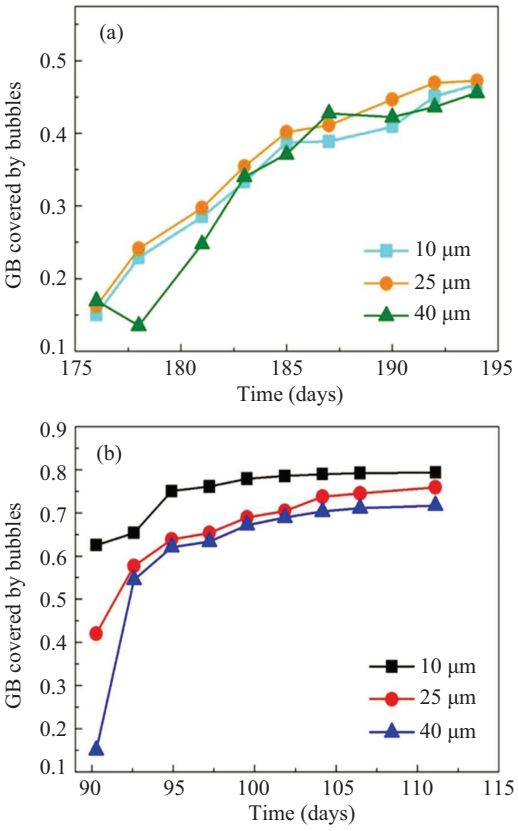


Fig. 13. Grain size effect on the fraction of intergranular bubbles in (a) UO_2 and (b) U_3Si_2.

Figure 13 shows the GBs covered by bubble as a function of time in UO_2 and U_3Si_2, respectively, under different

grain sizes. Relatively speaking, small grain size could induce more bubbles to form on the GBs. The porosity in UO_2 and U_3Si_2 with the smaller grain size is higher than that with the larger grain size, which is more obvious in the case of U_3Si_2 (Fig. 13(b)). The results of in-pile irradiation test also demonstrate that the large-grained UO_2 fuel can improve the irradiation swelling performance.[6,7] The intergranular porosity in the large-grained UO_2 is much lower than that in the small-grained one.[5] As aforementioned, GB is the trapping location of point defects and gas atom. More GB proportions mean more bubble formation on the GB. In addition, previously formed bubbles are preferred to trap point defects and fission gas atoms to accelerate bubble growth or shrinkage. In summary, UO_2 and U_3Si_2 with the mean grain size of 10 μm show higher bubble coverage than the microstructures with the grain sizes of 25 μm and 40 μm.

As is known, the thermal conductivity depends on the morphology of microstructure. On a basis of the phase-field simulated structure, we calculate the effective thermal conductivity of polycrystalline U_3Si_2. The effective thermal conductivity model and the thermal conductivities of the U_3Si_2 matrix and Xe bubble at 473 K, 673 K, and 873 K have been described in Subsection 3.2.1. The thermal conductivity of GB is used as 5 W/m·K in this study, which is the same as the previous work on polycrystalline UO_2 and U–Mo alloy.[42,43] Millett *et al.*[44] presented a general formula for estimating the effective thermal conductivity of polycrystals, and the specific expression is as follows:

$$\kappa^{\text{poly}} = \frac{\kappa_0}{1+[\kappa_0(1+\alpha(P_{\text{m}})^n)/G_{\text{k}}^0 d]}, \tag{23}$$

where P_{m} is the intergranular bubble occupancy, α and n are the fitting parameters, d is the mean grain size, G_{k}^0 is the Kalcha conductivity coefficient. If P_{m} is equal to zero, the values of β, G_{k}^0, and m are 0.0158, 156.76 MW/m^2·K, and 0.192, respectively, according to the fitted thermal conductivities related to different grain sizes. Consequently, the thermal conductivity considering grain size effect is given as

$$\kappa^{\text{poly}} = \frac{\kappa_0}{1+[0.0158\kappa_0/(156.76d)^{0.192}]}. \tag{24}$$

Figure 10 plots the effective thermal conductivity as functions of (a) grain size and (b) porosity. In Fig. 10(a), the effective thermal conductivity increases rapidly if the grain size is less than 10 μm; when the grain size exceeds 10 μm, the effective thermal conductivity increases in a slow rate. Different from grain size effect, the effective thermal conductivity varies with increasing porosity in a decrement. As expected, more gas bubbles are created in the microstructure with a smaller grain size, leading to a lower effective thermal conductivity as shown in Fig. 10(b). To quantitatively evaluate the porosity effect, the thermal conductivities of polycrystalline U_3Si_2 under the grain sizes of 10 μm, 25 μm, and 40 μm are described by the following expressions:

$$\kappa = 10.066 - 32.02p + 157.15p^2 - 424.28p^3, \tag{25}$$

$$\kappa = 10.178 - 41.1p + 377.03p^2 - 1508.68p^3, \tag{26}$$

$$\kappa = 10.172 - 18.25p + 52.16p^2 - 247.43p^3. \tag{27}$$

4. Conclusions

In this study, *ab initio* calculations are carried out to assess the stabilities of point defects and fission gas atom, and the phase-field model are established to simulate gas bubble evolution in both UO_2 and U_3Si_2. The stabilities of vacancy, interstitial atom and fission gas atom, the interaction between vacancy and fission gas atom, the role of temperature, fission rate, and grain size on the bubble evolution as well as the corresponding effective thermal conductivities of irradiated microstructures have systematically investigated. The main findings can be summarized as follows:

(i) The formation energy of vacancy and the incorporation energy of Xe atom in UO_2 are higher than those in U_3Si_2, and the vacancies can decrease the incorporation energy of Xe atom in both UO_2 and U_3Si_2.

(ii) Higher fission rate indicates that more point defects are generated in the fuel, leading to more bubbles formation. Hence, the porosity increases with the increment of fission rate.

(iii) The porosities of UO_2 and U_3Si_2 with 40-μm grain size are much lower than those in the smaller one, since the diffusion distance of fission gas atom from the interior grain to the GB increases in larger grain size.

(iv) The effective thermal conductivity strongly depends on the grain size, which influence the size and density of intergranular bubble. Higher porosity in the irradiated microstructure with smaller grain size can obviously degrade the thermal transfer capability.

Our comprehensive calculations enhance the understanding on the intra- and inter-granular gas bubble evolutions in UO_2 and U_3Si_2, which is critical for the prediction of gas swelling of large-grained fuel pellet.

Acknowledgments

Project supported by the National Natural Science Foundation of China (Grant Nos. U2167217, 12205286, and 11905025) and the National MCF Energy Research and Development Program of China (Grant No. 2018YFE0308105).

References

[1] Rebak R B 2020 *Accident-tolerant materials for light water reactor fuels* (Amsterdam: Elsevier) p. 45
[2] Gamble K A, Pastore G, Andersson D and Cooper M W 2019 *ATF material model development and validation for priority fuel concepts* (Idaho Falls: Idaho National Laboratory) p. 7

[3] Ortega L H, Blamer B J, Evans J A and McDeavitt S M 2016 *J. Nucl. Mater.* **471** 116
[4] Harp J M, Lessing P A and Hoggan R E 2015 *J. Nucl. Mater.* **466** 728
[5] Noirot J, Pontillon Y, Yagnik S and Turnbull J A 2015 *J. Nucl. Mater.* **46** 277
[6] Massih A 2014 *Effects of additives on uranium dioxide fuel behavior* (Uppsala: Swedish Radiation Safety Authority) p. 1
[7] Delafoy C and Dewes P 2006 *Top Fuel* 2006 *International Meeting on LWR Fuel Performance "Nuclear Fuel: Addressing the future"*, October 22–26, 2006, Salamance, Spain, pp. 142–146
[8] Cooper M W, Pastore G, Che Y, Matthews C, Forslund A, Stanek C R, Shirvan K, Tverberg T, Gamble K A, Mays B and Andersson D A 2021 *J. Nucl. Mater.* **545** 152590
[9] Gan J, Keiser D D Jr, Miller B D, Jue J F, Robinson A B, Madden J W, Medvedev P G and Wachs D M 2011 *J. Nucl. Mater.* **419** 97
[10] Barani T, Pastore G, Pizzocri D, Andersson D A, Matthews C, Alfonsi A, Gamble K A, Van Uffelen P, Luzzi L and Hales J D 2019 *J. Nucl. Mater.* **522** 97
[11] Shimizu H 1965 *The Properties and Irradiation Behavior of* U_3Si_2 (Canoga Park: Atomics International) NAA-SR-10621
[12] Miao Y, Gamble K A, Andersson D, Mei Z G and Yacout A M 2018 *Nucl. Eng. Des.* **326** 371
[13] Rest J 2003 *J. Nucl. Mater.* **325** 107
[14] Andersson D A, Liu X Y, Beeler B, Middleburgh S C, Claisse A and Stanek C R 2019 *J. Nucl. Mater.* **515** 312
[15] Yun Y, Kim H, Kim H and Park K 2008 *J. Nucl. Mater.* **378** 40
[16] Kaloni T P and Torres E 2020 *J. Nucl. Mater.* **533** 152090
[17] Millett P C, Tonks M R, Biner S B, Zhang L, Chockalingam K and Zhang Y 2012 *J. Nucl. Mater.* **425** 130
[18] Aagesen L K, Schwen D, Tonks M R and Zhang Y 2019 *Comput. Mater. Sci.* **161** 35
[19] Wang Y F, Z H Xiao and Shi S Q 2019 *Sci. Sin. Phys. Mech. Astron.* **49** 82
[20] Aagesen L K, Andersson D, Beeler B W, Cooper M W, Gamble K A, Miao Y, Pastore G and Tonks M R 2020 *J. Nucl. Mater.* **541** 152415
[21] Kresse G and Furthmüller J 1996 *Phys. Rev. B* **54** 11169
[22] Blöchl P E 1994 *Phys. Rev. B* **50** 17953
[23] Perdew J P, Chevary J A, Vosko S H, Jackson K A, Pederson M R, Singh D J and Fiolhais C 1992 *Phys. Rev. B* **46** 6671
[24] Dudarev S L, Botton G A, Savrasov S Y, Humphreys C J and Sutton A P 1998 *Phys. Rev. B* **57** 1505
[25] Liu X Y and Andersson A D 2018 *J. Nucl. Mater.* **498** 373
[26] Wang T, Qiu N, Wen X, Tian Y, He J, Luo K, Zha X, Zhou Y, Huang Q, Lang J and Du S 2016 *J. Nucl. Mater.* **469** 194
[27] Desgranges L, Baldinozzi G, Rousseau G, Niépce J C and Calvarin G 2009 *Inorg. Chem.* **48** 7585
[28] Vazhappilly T and Pathak A K 2019 *J. Nucl. Mater.* **519** 128
[29] Remschnig K, Le B T, Noël H and Rogl P 1992 *J. Solid State Chem.* **97** 391
[30] Millett P C, El-Azab A and Wolf D 2011 *Comput. Mater. Sci.* **50** 960
[31] Millett P C and Tonks M 2011 *Curr. Opin. Solid State Mater. Sci.* **15** 125
[32] Liang L, Mei Z G, Kim Y S, Anitescu M and Yacout A M 2018 *Comput. Mater. Sci.* **145** 86
[33] Xiao H X and Long C S 2013 *Chin. Phys. B* **23** 020502
[34] Beeler B, Baskes M, Andersson D, Cooper M W and Zhang Y 2019 *J. Nucl. Mater.* **514** 290
[35] Kashibe S, Une K and Nogita K 1993 *J. Nucl. Mater.* **206** 22
[36] Leenaers A, Van den Berghe S, Koonen E, Jacquet P, Jarousse C, Guigon B, Ballagny A and Sannen L 2004 *J. Nucl. Mater.* **327** 121
[37] Finlay M R, Hofman G L and Snelgrove J L 2004 *J. Nucl. Mater.* **325** 118
[38] Miao Y, Harp J, Mo K, Zhu S, Yao T, Lian J and Yacout A M 2017 *J. Nucl. Mater.* **495** 146
[39] Zhang Y, Beeler B, Aagesen L, Jiang C, Ahmed K, Yu J, Schwen D, Andersson D, Baskes M, Cooper M and Martinez E 2017 *Progress update on lower length scale research and development on* U_3Si_2 *fuel and FeCrAl cladding* (Idaho Falls: Idaho National Laboratory) p. 10
[40] Vargaftik N B and Yakush L V 1974 *J. Eng. Phys. Thermophys.* **21** 1156
[41] Bauer T H 1993 *Int. J. Heat Mass Transfer* **36** 4181
[42] Millett P C and Tonks M 2011 *J. Nucl. Mater.* **412** 281
[43] Hu S, Casella A M, Lavender C A, Senor D J and Burkes D E 2015 *J. Nucl. Mater.* **462** 64
[44] Millett P C, Tonks M R, Chockalingam K, Zhang Y and Biner S B 2013 *J. Nucl. Mater.* **439** 117